



1 **An iterative algorithm to simultaneously retrieve aerosol extinction and effective radius profiles using**  
2 **the CALIOP lidar**

3 Liang Chang<sup>1</sup>, Jing Li<sup>1, #</sup>, Jingjing Ren<sup>2</sup>, Changrui Xiong<sup>1</sup>, Lu Zhang<sup>3,4</sup>

4 <sup>1</sup> *Department of Atmospheric and Oceanic Sciences, School of Physics, Peking University, Beijing 100871,*  
5 *China*

6 <sup>2</sup> *Intelligent Science & Technology Academy Limited of CASIC*

7 <sup>3</sup> *Key Laboratory of Radiometric Calibration and Validation for Environmental Satellites, National Satellite*  
8 *Meteorological Center (National Center for Space Weather), China Meteorological Administration, Beijing*  
9 *100081, China*

10 <sup>4</sup> *Innovation Center for FengYun Meteorological Satellite (FYSIC), Beijing 100081, China*

11 *# Correspondence to: Jing Li (jing-li@pku.edu.cn)*

12

**Abstract**

13 The Cloud-Aerosol Lidar with Orthogonal Polarization (CALIOP) onboard the Cloud-Aerosol Lidar and  
14 Infrared Pathfinder Satellite Observation (CALIPSO) satellite has been widely used in climate and  
15 environment studies to obtain the vertical profiles of atmospheric aerosols. To retrieve the vertical profile of  
16 aerosol extinction, the CALIOP algorithm assumes column-averaged lidar ratios based on a clustering of  
17 aerosol optical properties measured at surface stations. On one hand, these lidar ratio assumptions may not  
18 be appropriate or representative at certain locations. On the other hand, the two-wavelength design of  
19 CALIOP has the potential to constrain aerosol size information, which has not been considered in the  
20 operational algorithm. In this study, we present a modified inversion algorithm to simultaneously retrieve  
21 aerosol extinction and effective radius profiles using two-wavelength elastic lidars such as the CALIOP.  
22 Specifically, a look-up table is built to relate the lidar ratio with the Ångström exponent calculated using  
23 aerosol extinction at the two wavelengths, and the lidar ratio is then determined iteratively without a priori



24 assumption. The retrieved two-wavelength extinction at each layer is then converted to particle effective  
25 radius assuming a lognormal distribution. The algorithm is tested on synthetic data, Raman lidar  
26 measurements and then finally the real CALIOP backscatter measurements. Results show improvements over  
27 the CALIPSO operational algorithm by comparing with ground-based Raman lidar profiles.

## 28 **1 Introduction**

29 Atmospheric aerosols have important impacts on the physical and chemical processes in atmosphere, as well  
30 as the climate system and public health. Optical properties of aerosols are critical in quantifying their radiative  
31 effects in the Earth's climate system. Moreover, the vertical distribution of aerosol properties, such as its  
32 extinction coefficient and particle size, is one of the key elements to assess climate effect (Ipcc, 2023). Direct  
33 aerosol radiative forcing, which plays an important role in the Earth's energy budget, is impacted by the  
34 vertical distribution of aerosols, especially that for absorbing aerosols (Goto et al., 2011; Eswaran et al., 2019;  
35 Zhang et al., 2022). The vertical profiles of aerosol optical properties is also essential estimating the solar  
36 heating rate (Kudo et al., 2016), and establishment of aerosol parameterization schemes for satellite remote  
37 sensing (He et al., 2016). Although its importance is widely recognized, aerosol vertical distribution is very  
38 difficult to monitor globally. Lidar is a major technique for obtaining the profiles of the aerosol properties,  
39 which has been used in ground-based and satellite remote sensing systems. Especially, spaceborne lidar is an  
40 effective way to observe the global distribution of aerosols. The Cloud-Aerosol Lidar with Orthogonal  
41 Polarization (CALIOP) on the CALIPSO (The Cloud-Aerosol Lidar and Infrared Pathfinder Satellite  
42 Observation) satellite, the only long-term orbiting spaceborne lidar to date, was launched on 28 April 2006.  
43 The CALIOP is a three-channel Mie-scattering lidar system, which contains two wavelengths of  $532nm$   
44 (perpendicular & parallel polarization channel) and  $1064nm$ . It is the first polarization lidar to provide three-  
45 channel elastic backscatter signals of global atmospheric measurements. The official aerosol retrieval  
46 algorithm of CALIOP involves three modules, namely the Selective Iterated BoundarY Locator (SIBYL),  
47 the Scene Classification Algorithm (SCA), and the Hybrid Extinction Retrieval Algorithms (HERA). The



48 HERA algorithm requires a lidar ratio (extinction-to-backscatter ratio of aerosols), which is provided by the  
49 SCA. The SCA uses three CALIOP channels (532nm parallel, 532nm perpendicular and 1064nm channels)  
50 to obtain the lidar ratio from the 6 groups of assumed column-averaged lidar ratios based on a clustering of  
51 aerosol optical properties measured at surface stations (Winker et al., 2009). However, due to the limited  
52 coverage and spatial representativeness of surface stations, these lidar ratio assumptions may not be  
53 appropriate or representative at certain locations (Josset et al., 2011), which is an important source of retrieval  
54 uncertainty.

55 The lidar ratio is dependent on the chemical composition, shape, particle size distribution of aerosols,  
56 as well as the lidar wavelength (Burton et al., 2012), which is a critical parameter required for solving the  
57 Mie-scattering lidar equation using the Klett (Klett, 1985) or Fernald (Fernald, 1984) methods. Previous  
58 studies have developed algorithms to determine the lidar ratio iteratively for two-wavelength Mie scattering  
59 lidars. Potter (1987) first introduced the two-wavelength lidar inversion technique to retrieve the aerosol  
60 transmission with a constant lidar ratio in two independent wavelengths. Ackermann (Ackermann, 1997,  
61 1998) developed an iterative method to obtain the variable lidar ratio from two-component (i.e., molecule  
62 and aerosol) atmospheres by transcendental equation. Rajeev and Parameswaran (1998) proposed a new  
63 method using the Mie theory calculated aerosol optical properties with Junge distribution of aerosols to  
64 determine the lidar ratio by iteration. Lu et al. (2011) made an attempt to improve the two-wavelength lidar  
65 inversion by iterative method, but failed to consider the size distribution of aerosols which may introduce  
66 uncertainties in the inversion. Moreover, these studies mostly only gave the aerosol extinction profile without  
67 retrieving the vertical distribution of aerosol size information. The algorithms were also mostly applied to  
68 theoretical data or ground lidar measurements. The application to space lidars such as CALIOP is challenging  
69 and thus limited.

70 In view of the above discussions, this study aims to provide a modified two-wavelength lidar  
71 inversion algorithm to retrieve the vertical distribution of both aerosol extinction and particle effective radius,  
72 avoiding the complex calculation confronted in the previous two-wavelength lidar inversion methods. The



73 algorithm is tested on synthetic data, surface Raman lidar and is finally applied to CALIOP measurements,  
74 in order to better demonstrate its operational feasibility. The paper proceeds with descriptions of the inversion  
75 algorithm in Sect. 2. Sect. 3 presents the application of the algorithm to the Raman lidar and CALIOP with  
76 an analysis of retrieval uncertainties provided in Sect. 4. The study concludes in Sect. 5 with a brief discussion  
77 in the context of relevant lidar algorithms.

## 78 **2 Description of the lidar inversion algorithm**

79 The modified inversion algorithm retrieves the profiles of aerosol extinction and effective radius at two  
80 wavelengths, by solving the lidar equation using the Fernald method (Fernald, 1984) with a look-up table.

### 81 **2.1 Solving the lidar equation**

82 For each wavelength with a complete overlap between the fields of view of the laser and of the receiver, the  
83 lidar equation with calibration and range-correction can be expressed as:

$$84 \quad \beta'(R) = \frac{P(R)R^2}{E_0\xi} = [\beta_m(R) + \beta_p(R)]T_m^2(R)T_p^2(R), \quad (1)$$

85 where

$$86 \quad T^2(R) = e^{-2\tau(R)}, \quad (2)$$

$$87 \quad \tau(R) = \int_{R_0}^R \sigma(r)dr, \quad (3)$$

88 In Eq. (1-3),  $\beta'(R)$  is the attenuated backscatter coefficients (calibrated and range-corrected signal)  
89 from distance  $R$ ;  $P(R)$  is the measured signal after background subtraction and artefact removal from  
90 distance  $R$ ;  $E_0$  is the average laser energy for the single-shot;  $\xi$  is the lidar system parameter;  $\beta(R)$  and  $\sigma(R)$   
91 are the volume backscatter and extinction coefficient at range  $R$ , respectively;  $T^2(R)$  is the one-way  
92 transmittance from the lidar to the scattering volume at range  $R$ ;  $\tau(R)$  is the optical depth at range  $R$ ; and the  
93 subscripts  $M$  and  $P$  denote the portions of air molecules and aerosols, respectively.

94 In order to facilitate calculation, the transmittance of air molecules  $T_m^2(R)$  is separated from  $\beta'(R)$   
95 to obtain the  $E(R)$  as



$$96 \quad E(R) = \frac{\beta'(R)}{T_m^2(R)}, \quad (4)$$

97 As is well known, lidar back scatter signal is also subject to multiple scattering effects. These effects  
 98 are typically small for low to moderate aerosol loading, and is only significant for optically thick clouds [7].  
 99 Therefore, we neglect multiple scattering effects here and consider that the lidar ratio ( $S(R)$ ) of aerosols is  
 100 range dependent in single-scatter approximation, which can be written as

$$101 \quad S(R) = \frac{\sigma_p(R)}{\beta_p(R)}, \quad (5)$$

102 In the following, we use the Fernald method (Ackermann, 1998) to obtain the aerosol extinction  
 103 coefficient at distance  $R$  as

$$104 \quad \sigma_p(R) = S(R) \left\{ E(R) e^{-2 \int_{R_0}^R S(r) \beta_m(r) dr} \left[ C - 2 \int_{R_0}^R E(r) S(r) e^{-2 \int_{R_0}^r S(r') \beta_m(r') dr'} dr \right]^{-1} - \beta_m(R) \right\}, \quad (6)$$

105 where

$$106 \quad C = \frac{\beta'(R_0)}{\beta_p(R_0) + \beta_m(R_0)}, \quad (7)$$

107 The backscatter and extinction coefficient of air molecules can be determined with the Rayleigh  
 108 scattering theory with the observed atmospheric profile (Bodhaine et al., 1999) as

$$109 \quad \sigma_m(R, \lambda) = \frac{C_s(\lambda) P(R)}{T(R)}, \quad (8)$$

$$110 \quad \beta_m(R, \lambda) = \frac{\sigma_m(R, \lambda)}{\frac{8\pi}{3} k_{b\omega}(\lambda)}, \quad (9)$$

111 Where  $P(R)$  and  $T(R)$  are the atmospheric pressure ( $hPa$ ) and temperature ( $K$ ) at distance  $R$ , respectively.  
 112  $C_s(\lambda)$  and  $k_{b\omega}(\lambda)$  are the atmospheric molecular constant related to the wavelength  $\lambda$ . Hostetler et al. (2006)  
 113 suggested the values of  $C_s(\lambda)$  and  $k_{b\omega}(\lambda)$  at  $532nm$  and  $1064nm$  as  $C_s(532nm) = 3.742 \times 10^{-6} (K/hPa/m)$ ;  
 114  $C_s(1064nm) = 2.265 \times 10^{-7} (K/hPa/m)$ ;  $k_{b\omega}(532nm) = 1.0313$ ;  $k_{b\omega}(1064nm) = 1.0302$ .

115 Thus, the aerosol extinction coefficient profiles can be obtained by Eq. (6) with an unknown variable  
 116 of the lidar ratio. The two-wavelength lidar can give two independent profiles of attenuated backscatter



117 coefficients, from which the aerosol extinction coefficient profiles can be calculated by assuming the lidar  
118 ratios at the two wavelengths.

119 For two wavelengths ( $\lambda_1$  &  $\lambda_2$ ), the Ångström exponent ( $AE$ ) at distance  $R$  is defined as:

$$120 \quad AE(R) = -\frac{\ln\left[\frac{\sigma_p(R, \lambda_1)}{\sigma_p(R, \lambda_2)}\right]}{\ln\left[\frac{\lambda_1}{\lambda_2}\right]}, \quad (10)$$

121 Because  $AE$  is related to particle effective radius, which is a primary factor determining the lidar ratio,  
122 an  $AE$ -lidar ratio relationship can be established and used to determine the lidar ratio at each layer, which can  
123 then be used to retrieve aerosol extinction profiles from two-wavelength lidar measurements.

## 124 2.2 Look-up table

125 By assuming spherical particles with some size distribution, the aerosol extinction coefficients and  
126 backscatter coefficients can be calculated by Eq. (11-12):

$$127 \quad \sigma_p(\lambda) = \int_{r_{min}}^{r_{max}} Q_e(\lambda, r) \pi r^2 n(r) dr, \quad (11)$$

$$128 \quad \beta_p(\lambda) = \int_{r_{min}}^{r_{max}} Q_b(\lambda, r) \pi r^2 n(r) dr, \quad (12)$$

129 Where  $n(r)$  represents the volume-size distribution of particles;  $r_{max}$  and  $r_{min}$  are the maximum and  
130 minimum of the particle effective radius, respectively;  $Q_e(\lambda, r)$  and  $Q_b(\lambda, r)$  denote the extinction efficiency  
131 and backscatter factor of the particle with size  $r$  at wavelength  $\lambda$ . The size parameter is defined as  $x \equiv 2\pi r /$   
132  $\lambda$ , where  $1 < x < 50$  for typical aerosols and thus the Mie scattering theory can be applied.

133 As the limited information provided by two-wavelength lidar, we assume the volume-size distribution  
134 of aerosols conform to the lognormal distribution, and the size distribution is expressed as follows:

$$135 \quad n(r) = \frac{N}{\sqrt{2\pi}s_d} e^{-\frac{(r-\bar{r})^2}{2s_d^2}}, \quad (13)$$

136 Where  $N$  is the total particle concentration;  $\bar{r}$  is the average particle radius;  $s_d$  is the standard deviation.  
137 When the  $s_d$  is a constant in the same aerosol, the  $AE$  can be determined by the  $r$ .

138 We choose the six types of aerosols with their parameters in Table 1, which is consistent with the  
139 aerosol classification used in the operational algorithm of CALIOP. From Table 1, Type 3 denotes the



140 scattering aerosols, Type 2 shows both strong scattering and absorption, whereas other types are moderate  
141 scattering or absorbing. Combining Eqs. (5, 10-13), the relationship between Ångström exponent ( $AE$ ) and  
142 lidar ratio ( $S$ ), as well as that between  $AE$  and particle effective radius ( $r$ ) can be formulated as look-up tables  
143 for different refractive indices, as shown in Figure 1. Note that in Figure 1, it is easy to determine  $S_{532nm}$ ,  
144  $S_{1064nm}$  and  $\bar{r}$  by the unique  $AE$  calculated from the lidar equation for a fixed aerosol type.

### 145 **2.3 The iterative inversion procedure**

146 After constructing the look-up table, we design the following iterative procedure to simultaneously retrieve  
147 aerosol extinction and effective radius profiles. Firstly, we calculate the extinction coefficients ( $\sigma_{532nm}$  &  
148  $\sigma_{1064nm}$ ) of two wavelengths (532nm & 1064nm) from an initial guess of the lidar ratios ( $S_{532nm}^0$  &  
149  $S_{1064nm}^0$ ) by solving the lidar equation (Eq. 6), then obtain the Ångström exponent ( $AE$ ) through Eq. (10).  
150 Secondly, the look-up table are used to determine a set of new lidar ratios ( $S'_{532nm}$  &  $S'_{1064nm}$ ), which is used  
151 to calculate the new  $\sigma_{532nm}$  &  $\sigma_{1064nm}$  and Ångström exponent ( $AE'$ ). This procedure is repeated until the  
152 difference between the updated  $AE'$  and previous  $AE$  reduces to a very small value (e.g.,  $10^{-3}$ ). The final  $AE$   
153 is converted to effective radius from the  $AE$ - $\bar{r}$  look-up table, and the final values of  $\sigma_{532nm}$ ,  $\sigma_{1064nm}$ , and  $\bar{r}$   
154 are the retrieved results of this layer. The above iterative algorithm is summarized into Figure 2.

155         Although in theory, our algorithm can retrieve aerosol extinction and effective radius at each layer,  
156 in reality the measurement noise may cause the inversion of certain layers fail to converge. In these cases,  
157 we assume that this layer has the same aerosol type and size distribution as its adjacent layer, and then these  
158 two layers are combined into a new layer to continue with the inversion.

### 159 **2.4 Test of the algorithm with synthetic data**

160 For verifying the feasibility of the inversion algorithm, we first conduct some retrieval tests using synthetic  
161 data from Mie scattering and radiative transfer simulations. We assume a hypothesized profile of effective  
162 radius, backscatter and extinction coefficients of the aerosols, and use the American atmospheric model in  
163 1976 (National Geophysical Data, 1992) for molecular scattering, and calculate the attenuated backscatter



164 profiles according to the lidar equation. We then apply our algorithm to retrieve the aerosol property profiles  
165 from these simulated lidar signals and compare them with the initial assumptions.

166 To save space, we only present the results for the reflective aerosol model, and results for other aerosol  
167 types are similar. The simulated attenuated backscatter profiles for the two wavelengths are shown in Figure  
168 3, and the results of our inversion and their comparison with the assumed profiles are shown in Figure 4. It  
169 is clearly seen that the results of the inversion are in good agreement with the assumed profiles. The RRMSE  
170 (Relative Root Mean Square Error) between retrieved and assumed profiles of extinction coefficient, average  
171 particle effective radius and lidar ratio are all below 0.01%, which proves the validity of the algorithm in  
172 theory. Note that typically, selection of aerosol type is critical as incorrect assumption of aerosol refractive  
173 index will result in divergence of the algorithm and thus yield no valid retrieval.

### 174 **3 Application to real lidar measurements**

175 Before applying our algorithm to CALIOP measurements, we first use Raman lidar measurements to test its  
176 accuracy as Raman lidars can directly retrieve aerosol extinction profiles without assuming a lidar ratio.

#### 177 **3.1 Application to Raman lidar measurements**

178 A Raman lidar (Model LR231-D300, Raymetrics S.A, Greece) is installed on top of an 8-floor building at  
179 the Peking University site (39°59'N, 116°18'E, 53m above sea level). It can provide the extinction and  
180 backscatter coefficient at 532nm by Raman inversion (Ansmann et al., 1990) without the need to assume the  
181 lidar ratio. To test our inversion algorithm, we apply it to the elastic backscatter signals at 532 and 1064nm  
182 and compare the retrieved extinction profile at 532nm with that retrieved with the Raman method. but an  
183 approximation of  $AE$  is used in the inversion at 1064nm. We apply the modified inversion algorithm to  
184 the cases of four different aerosol types. To facilitate the determination of the initial value, we use the method  
185 of remodelling downward attenuated backscatter from ground-based lidar (Tao et al., 2008) to reconstruct  
186 the Raman lidar measurements at wavelength of 532nm and 1064nm, which are showing Figure 5-8(a).





187 We examined four cases in December 2017, as shown in Figures 5-8. The cases on 2 and 21 December 2017  
188 both indicate that the extinction coefficient decreases sharply with altitude, and the maximum values occur  
189 near the ground (Figure 6b & 7b). The other two cases on December 1 and 23 respectively show the features  
190 of an elevated aerosol layer with maximum extinction found above the surface. In all four cases, our retrieval  
191 results (red curves) agree well with those retrieved by the Raman method, with RMSE lower than 0.05. The  
192 lidar ratio profiles retrieved by our algorithm also agree well with obtained from Raman method in some  
193 ranges, except these spikes at the highest or lowest point, may be caused by the uncertainty of boundary. The  
194 aerosol particle effective radius slightly increases with altitude and the peak (corresponding to  $\sim 0.1\mu\text{m}$ )  
195 appear at  $\sim 0.7\text{km}$  and  $\sim 1.7\text{km}$  on 1 and 23 December 2017 (Figure 5d & 8d), respectively. Similar results  
196 were found by Zhang et al. (2009) and Cai et al. (2022) with aircraft measurements over Beijing and the  
197 Loess Plateau in China respectively, which are mainly associated with long range aerosol transport. The  
198 variability of particle effective radius profiles in Figure 6d is a typical feature for low (and stable) PBL  
199 (Planetary Boundary Layer), which results in both particles and water vapor accumulating near PBL top and  
200 thus remarkable hygroscopic growth of particle size may occur (Yang et al., 2020). The case for Dec 21  
201 (Figure 7d) shows relatively large particle size below  $\sim 1.4\text{km}$  but sharply decreases. This is likely related to  
202 the domination of local pollutions and insignificant PBL temperature inversion (Li et al., 2022; Liu et al.,  
203 2009; Zhang et al., 2009).

### 204 **3.2 Application to CALIOP measurements**

205 We further apply our algorithm to real CALIOP measurements. To test its performance, we collocate  
206 CALIOP profiles with those from surface-based Raman lidar measurement within the European Aerosol  
207 Research Lidar NETwork (EARLINET, [www.earlinet.org](http://www.earlinet.org), (Matthias et al., 2004). Aerosol profiles from the  
208 Napoli (southern Italy,  $40.838^\circ\text{N}$ ,  $14.183^\circ\text{E}$ , 118m above sea level), Evora (south-central  
209 Portugal,  $38.5678^\circ\text{N}$ ,  $-7.9115^\circ\text{E}$ , 293m above sea level) and Warsaw (east-central,  $52.21^\circ\text{N}$ ,  $20.98^\circ\text{E}$ ,  
210 112m above sea level) stations have the best match with CALIOP and high data quality in cloudless sky, are  
211 primarily used to validate the retrieval results. The CALIPSO overpass times for the chosen cases and the



212 corresponding horizontal distances between the sub-satellite point and ground-based Raman lidar site are  
213 listed in Table 2.

214 To compare with the lidar returns measured by CALIOP (down-looking) and ground-based Raman  
215 lidar (up-looking), we still use the method of remodelling downward attenuated backscatter from ground-  
216 based lidar (Tao et al., 2008) to reconstruct the downward attenuated backscatter signals for the ground-based  
217 Raman lidar. The attenuated backscatter signals of CALIOP was averaged for 163 nearby sub-satellite point  
218 profiles (CALIPSO ground track range of about 30km within 8s) (Lu et al., 2011; Wang et al., 2007), obtained  
219 from CALIOP level 1B products, to improve the signal-to-noise ratio.

220 The attenuated backscatter profiles at  $532\text{nm}$  from CALIOP agree well with those from the Napoli  
221 Raman Lidar (NRL), as shown in Figures 9-14(a). The initial altitude of inversion (the upper boundary of the  
222 aerosol layer) is determined by the variation of attenuated backscatter signal and volume linear depolarization  
223 ratio at  $532\text{nm}$ . Comparison between our inversion results, CALIOP operational results and Raman results  
224 is shown in Figure 9-14(c).

225 The CALIOP operational product only provides retrievals for three cases considered, namely 20  
226 August 2006, 20 June 2007 and 22 July 2007. In all three cases, the aerosol extinction profiles of our  
227 algorithm (red curve) appear in better consistency with Raman lidar results. Our algorithm successfully  
228 corrects the overestimation for the August 20 2006 and July 22, 2007 cases. For the June 20, 2007 case, the  
229 operational results show a lower peak at  $\sim 1.7\text{km}$  and a secondary peak at  $\sim 4\text{km}$ , both of which are absent in  
230 the Raman profile, and our results agree well with Raman in both the shape and magnitude. In the other three  
231 cases, CALIOP does not provide Level 2 retrieval results. Our algorithm is able to retrieve and the extinction  
232 profiles agree well with Raman lidar observations. Our retrievals do show more fluctuations compared to  
233 Raman lidar, possibly due to the noises in the attenuated backscatter profiles of CALIOP. Because Raman  
234 lidar does not provide retrieval of aerosol effective radius profiles, we compare the lidar ratio profiles by our  
235 algorithm and the Raman algorithm. Overall, our algorithm produces lidar ratios varying in a relatively small  
236 range around 50, whereas Raman lidar ratios can vary from  $\sim 10$  to 200. Also, the Raman lidar ratios tend to



237 change sharply at the highest or lowest point, which may be caused by the inversion errors at the boundary.  
238 By removing these spikes, the differences of the lidar ratio between CALIOP and Raman is obviously reduced.  
239 In general, the aerosol particle effective radius increases with altitude, similar to Figures 5d and 8d, but the  
240 fluctuations of the profiles may also be caused the noise in the CALIOP measurement.

241 When examining the CALIOP backscatter measurements, we found that the backscatter signal at  
242 1064nm is often stronger than that at 532nm after 2010, which is unphysical and possibly due to issues such  
243 as calibration and lidar degradation. As a result, the remodeled backscatter profiles of CALIOP appear noisier  
244 and do not exactly match those from Raman lidar for the Evora and Warsaw stations, which only have  
245 collocated measurements in 2019 and 2020 (Figure 15-19a). Our retrieved extinction profiles also agree  
246 reasonably well with those by Raman lidar (Figure 15-19b), with the lidar ratio profiles and aerosol particle  
247 effective radius profiles similar to the cases at Naples. By contrast, the extinction profiles of the official  
248 CALIPSO product show large deviations from the Raman profile with unphysical spikes (Figure 16b),  
249 incomplete profiles (Figure 17&18b) or no retrievals (Figure 15b).

#### 250 **4 Uncertainty analysis**

251 Uncertainties in aerosol extinction and effective radius profiles from our two-wavelength inversion algorithm  
252 are mainly due to the measurement noise (e.g., the signal statistical error, the estimations of molecular optical  
253 properties, etc.), calibration errors, assumption errors (e.g., single-scatter approximation) and the look-up  
254 table. In this section, we mainly analyze the errors associated with the look-up table.

255 Since the value of  $AE$ , which is the key variable in the iterative process, is obtained from the look-up  
256 table, the errors on the hypothesis of aerosol refractive index, size distribution and shape in each aerosol layer  
257 will affect the variability of lidar ratio in solving the lidar equation. Figure 20 shows the relationship between  
258 spherical aerosol particle radius and  $AE$  in different aerosol refractive indices. For aerosol particles with the  
259 same size, the real part of the refractive index ( $m_r$ ) mainly affects the cycle period of  $AE$ , and the imaginary  
260 part ( $m_i$ ) directly impacts its range of variability. In addition,  $AE$  is not quite sensitive to coarse particles,



261 which limit the applicability of our algorithm primarily to fine mode aerosols. The spherical assumption also  
262 adds to the uncertainty in the existence of non-spherical particles, such as dust.

263 Although the significant difference of these six aerosol types in look-up table can ensure the reasonable  
264 inversion result come from a specific aerosol type, the limited look-up table also restrict the inversion of  
265 other aerosol types. As the different type of aerosols in the aerosols optical parameters database of CEOS-  
266 Chem (<http://wiki.seas.harvard.edu/geos-chem>) show that the relative change of complex imaginary parts of  
267 refractive index is greater than its real parts (e.g. at  $532nm$ :  $1.3 < m_r < 1.7$  &  $0 < m_i < 0.4$ ), which tells  
268 our look-up table need to pay more attention to the complex imaginary parts of refractive index in the future.

## 269 **5 Summary and discussion**

270 In this study, we described a modified lidar inversion algorithm to retrieve aerosol extinction and size  
271 distribution simultaneously from two wavelengths elastic lidar measurements. Its major advantage over the  
272 operational CALIOP algorithm is that the lidar ratio of each layer is determined iteratively by the lidar ratio-  
273 AE look-up table. The algorithm was applied to the ground-based Raman lidar measurements at the PKU  
274 site, as well as to CALIOP measurements. The comparison results indicate that the retrieved aerosol  
275 extinction coefficient profiles by our method using CALIOP attenuated backscatter measurements are in  
276 good agreement with Raman lidar measurements. Characteristics of aerosol effective radius profiles are also  
277 retrieved, which can be used as a reference for aerosols size information.

278 In comparison with the iterative method by transcendental equation (Ackermann, 1997, 1998), our  
279 inversion uses the look-up table to simplify the complex calculation. Cao et al. (2019) develop a lidar-ratio  
280 iteration method to invert the particle-size distribution with assumed Junge distribution, but the method was  
281 just used in simple simulation without actual tests. Although Lu et al. (2011) invert the aerosol backscatter  
282 coefficient profiles from CALIPSO lidar measurements by iterative method, failed to consider the size  
283 distribution of aerosols which may introduce uncertainties in the inversion. Compared with other modified



284 CALIOP inversions by combining other measurements, such as ground-based lidar (Wang et al., 2007), our  
285 inversion is weaker by the space-time limitations.

286         However, this study still bears certain limitations. The current algorithm is primarily suitable for fine  
287 mode spherical particles, such as urban pollution, and considers the change of aerosol size (thus lidar ratio)  
288 with altitude, due to long range transport, vertical mixing, hygroscopic growth, etc. Non-spherical particles  
289 such as dust will be explored in the next step, possible by taking advantage of the depolarization ratio  
290 measurement that is not used here. Another drawback is that although the algorithm does not need to assume  
291 a lidar ratio, the complex refractive index still needs to be assumed. As discussed above, the lidar ratio is  
292 very sensitive to the imaginary part and an incorrect assumption may induce errors or even makes the  
293 algorithm unable to converge. Therefore, this algorithm is mostly suitable when there is no significant change  
294 in aerosol type vertically. Finally, the polarization channel of CALIOP may contain additional aerosol type  
295 information but is only used when determining the initial refractive index (excluding dust) here. We also plan  
296 to refine our look-up table by incorporating polarization in order to improve the accuracy of the retrieval.

#### 297 **Data availability**

298 All raw data can be provided by the corresponding authors upon request.

#### 299 **Author contributions**

300 LC and JL planned the research; LC, JL, JR, CX, and LZ developed the algorithm; LC and JL analyzed the  
301 results; LC and JL wrote the manuscript.

#### 302 **Competing interests**

303 The authors declare that they have no conflict of interest.



304 **Acknowledgement**

305 This study is funded by National Natural Science Foundation of China (NSFC) Grant No. 42175144.



## 306 References

- 307 Ackermann, J.: Two-wavelength lidar inversion algorithm for a two-component atmosphere, *Appl. Opt.*, 36,  
308 5134-5143, 10.1364/AO.36.005134, 1997.
- 309 Ackermann, J.: Two-wavelength lidar inversion algorithm for a two-component atmosphere with variable  
310 extinction-to-backscatter ratios, *Appl. Opt.*, 37, 3164-3171, 10.1364/AO.37.003164, 1998.
- 311 Ansmann, A., Riebesell, M., and Weitkamp, C.: Measurement of atmospheric aerosol extinction profiles with  
312 a Raman lidar, *Opt. Lett.*, 15, 746-748, 10.1364/OL.15.000746, 1990.
- 313 Bodhaine, B. A., Wood, N. B., Dutton, E. G., and Slusser, J. R.: On Rayleigh Optical Depth Calculations,  
314 *Journal of Atmospheric and Oceanic Technology*, 16, 1854-1861, 10.1175/1520-  
315 0426(1999)016<1854:orodc>2.0.co;2, 1999.
- 316 Burton, S. P., Ferrare, R. A., Hostetler, C. A., Hair, J. W., Rogers, R. R., Obland, M. D., Butler, C. F., Cook,  
317 A. L., Harper, D. B., and Froyd, K. D.: Aerosol classification using airborne High Spectral Resolution  
318 Lidar measurements – methodology and examples, *Atmos. Meas. Tech.*, 5, 73-98, 10.5194/amt-5-73-  
319 2012, 2012.
- 320 Cai, Z., Li, Z., Li, P., Li, J., Sun, H., Yang, Y., Gao, X., Ren, G., Ren, R., and Wei, J.: Vertical distributions  
321 of aerosol microphysical and optical properties based on aircraft measurements made over the Loess  
322 Plateau in China, *Atmospheric Environment*, 270, 118888,  
323 <https://doi.org/10.1016/j.atmosenv.2021.118888>, 2022.
- 324 Cao, N., Yang, S., Cao, S., Yang, S., and Shen, J.: Accuracy calculation for lidar ratio and aerosol size  
325 distribution by dual-wavelength lidar, *Applied Physics A*, 125, 590, 10.1007/s00339-019-2819-y,  
326 2019.
- 327 Eswaran, K., Satheesh, S. K., and Srinivasan, J.: Sensitivity of aerosol radiative forcing to various aerosol  
328 parameters over the Bay of Bengal, *Journal of Earth System Science*, 128, 170, 10.1007/s12040-019-  
329 1200-z, 2019.



- 330 Fernald, F. G.: Analysis of atmospheric lidar observations: some comments, *Appl. Opt.*, 23, 652-653,  
331 10.1364/AO.23.000652, 1984.
- 332 Goto, D., Nakajima, T., Takemura, T., and Sudo, K.: A study of uncertainties in the sulfate distribution and  
333 its radiative forcing associated with sulfur chemistry in a global aerosol model, *Atmos. Chem. Phys.*,  
334 11, 10889-10910, 10.5194/acp-11-10889-2011, 2011.
- 335 He, Q., Li, C., Geng, F., Zhou, G., Gao, W., Yu, W., Li, Z., and Du, M.: A parameterization scheme of aerosol  
336 vertical distribution for surface-level visibility retrieval from satellite remote sensing, *Remote  
337 Sensing of Environment*, 181, 1-13, <https://doi.org/10.1016/j.rse.2016.03.016>, 2016.
- 338 Hostetler, C., Liu, Z., Reagan, J., Vaughan, M., Winker, D., Osborn, M., Hunt, W., Powell, K., and Trepte,  
339 C.: CALIOP algorithm theoretical basis document calibration and Level 1 data products, Hampton,  
340 VA: NASA Langley Research Center, 2006.
- 341 IPCC: Climate Change 2021 – The Physical Science Basis: Working Group I Contribution to the Sixth  
342 Assessment Report of the Intergovernmental Panel on Climate Change, Cambridge University Press,  
343 Cambridge, DOI: 10.1017/9781009157896, 2023.
- 344 Josset, D., Rogers, R., Pelon, J., Hu, Y., Liu, Z., Omar, A., and Zhai, P.-W.: CALIPSO lidar ratio retrieval  
345 over the ocean, *Opt. Express*, 19, 18696-18706, 10.1364/OE.19.018696, 2011.
- 346 Klett, J. D.: Lidar inversion with variable backscatter/extinction ratios, *Appl. Opt.*, 24, 1638-1643,  
347 10.1364/AO.24.001638, 1985.
- 348 Kudo, R., Nishizawa, T., and Aoyagi, T.: Vertical profiles of aerosol optical properties and the solar heating  
349 rate estimated by combining sky radiometer and lidar measurements, *Atmos. Meas. Tech.*, 9, 3223-  
350 3243, 10.5194/amt-9-3223-2016, 2016.
- 351 Li, Y., Guo, X., Jin, L., Li, P., Sun, H., Zhao, D., and Ma, X.: Aircraft Measurements of Summer Vertical  
352 Distributions of Aerosols and Transitions to Cloud Condensation Nuclei and Cloud Droplets in  
353 Central Northern China, *Chinese Journal of Atmospheric Sciences*, 46, 845, 10.3878/j.issn.1006-  
354 9895.2104.20255, 2022.





- 355 Liu, P., Zhao, C., Zhang, Q., Deng, Z., Huang, M., Ma, X., and Tie, X.: Aircraft study of aerosol vertical  
356 distributions over Beijing and their optical properties, *Tellus B*, 61, 756-767,  
357 <https://doi.org/10.1111/j.1600-0889.2009.00440.x>, 2009.
- 358 Lu, X., Jiang, Y., Zhang, X., Wang, X., and Spinelli, N.: Two-wavelength lidar inversion algorithm for  
359 determination of aerosol extinction-to-backscatter ratio and its application to CALIPSO lidar  
360 measurements, *Journal of Quantitative Spectroscopy and Radiative Transfer*, 112, 320-328,  
361 <https://doi.org/10.1016/j.jqsrt.2010.07.013>, 2011.
- 362 Matthias, V., Freudenthaler, V., Amodeo, A., Balin, I., Balis, D., Bosenberg, J., Chaikovsky, A., Chourdakis,  
363 G., Comeron, A., Delaval, A., De Tomasi, F., Eixmann, R., Hagard, A., Komguem, L., Kreipl, S.,  
364 Matthey, R., Rizi, V., Rodrigues, J., Wandinger, U., and Wang, X.: Aerosol lidar intercomparison in  
365 the framework of the EARLINET project. 1. Instruments (vol 43, pg 976, 2004), *Appl. Opt.*, 43, 2004.
- 366 National Geophysical Data, C.: U.S. standard atmosphere (1976), *Planetary and Space Science*, 40, 553-554,  
367 [https://doi.org/10.1016/0032-0633\(92\)90203-Z](https://doi.org/10.1016/0032-0633(92)90203-Z), 1992.
- 368 Potter, J. F.: Two-frequency lidar inversion technique, *Appl. Opt.*, 26, 1250-1256, 10.1364/AO.26.001250,  
369 1987.
- 370 Rajeev, K. and Parameswaran, K.: Iterative method for the inversion of multiwavelength lidar signals to  
371 determine aerosol size distribution, *Appl. Opt.*, 37, 4690-4700, 10.1364/AO.37.004690, 1998.
- 372 Tao, Z., McCormick, M. P., and Wu, D.: A comparison method for spaceborne and ground-based lidar and  
373 its application to the CALIPSO lidar, *Applied Physics B*, 91, 639, 10.1007/s00340-008-3043-1, 2008.
- 374 Wang, X., Frontoso, M. G., Pisani, G., and Spinelli, N.: Retrieval of atmospheric particles optical properties  
375 by combining ground-based and spaceborne lidar elastic scattering profiles, *Opt. Express*, 15, 6734-  
376 6743, 10.1364/OE.15.006734, 2007.
- 377 Winker, D. M., Vaughan, M. A., Omar, A., Hu, Y., Powell, K. A., Liu, Z., Hunt, W. H., and Young, S. A.:  
378 Overview of the CALIPSO Mission and CALIOP Data Processing Algorithms, *Journal of*  
379 *Atmospheric and Oceanic Technology*, 26, 2310-2323, 10.1175/2009jtecha1281.1, 2009.



380 Yang, J., Li, J., Li, P., Sun, G., Cai, Z., Yang, X., Cui, C., Dong, X., Xi, B., Wan, R., Wang, B., and Zhou,  
381 Z.: Spatial Distribution and Impacts of Aerosols on Clouds Under Meiyu Frontal Weather  
382 Background Over Central China Based on Aircraft Observations, *Journal of Geophysical Research:*  
383 *Atmospheres*, 125, e2019JD031915, <https://doi.org/10.1029/2019JD031915>, 2020.

384 Zhang, L., Li, J., Jiang, Z., Dong, Y., Ying, T., and Zhang, Z.: Clear-Sky Direct Aerosol Radiative Forcing  
385 Uncertainty Associated with Aerosol Optical Properties Based on CMIP6 Models, *Journal of Climate*,  
386 35, 3007-3019, <https://doi.org/10.1175/JCLI-D-21-0479.1>, 2022.

387 Zhang, Q., Ma, X., Tie, X., Huang, M., and Zhao, C.: Vertical distributions of aerosols under different  
388 weather conditions: Analysis of in-situ aircraft measurements in Beijing, China, *Atmospheric*  
389 *Environment*, 43, 5526-5535, <https://doi.org/10.1016/j.atmosenv.2009.05.037>, 2009.

390

391



392 **Table 1.** The aerosols parameters of the look-up table.  $m_r$  denotes the real part of the refractive index,  $m_i$   
393 denotes the imaginary part of the refractive index, and  $s_d$  is the standard deviation of the lognormal size  
394 distribution.

395

	Type 1	Type 2	Type 3	Type 4	Type 5	Type 6
$m_r$ (532nm)	1.414	1.517	1.380	1.404	1.400	1.452
$m_i$ (532nm)	0.0036	0.0234	0.0001	0.0063	0.0050	0.0109
$m_r$ (1064nm)	1.495	1.541	1.380	1.439	1.400	1.512
$m_i$ (1064nm)	0.0043	0.0298	0.0001	0.0073	0.0050	0.0137
$s_d$	1.4813	1.5624	1.6100	1.5257	1.6000	1.5112

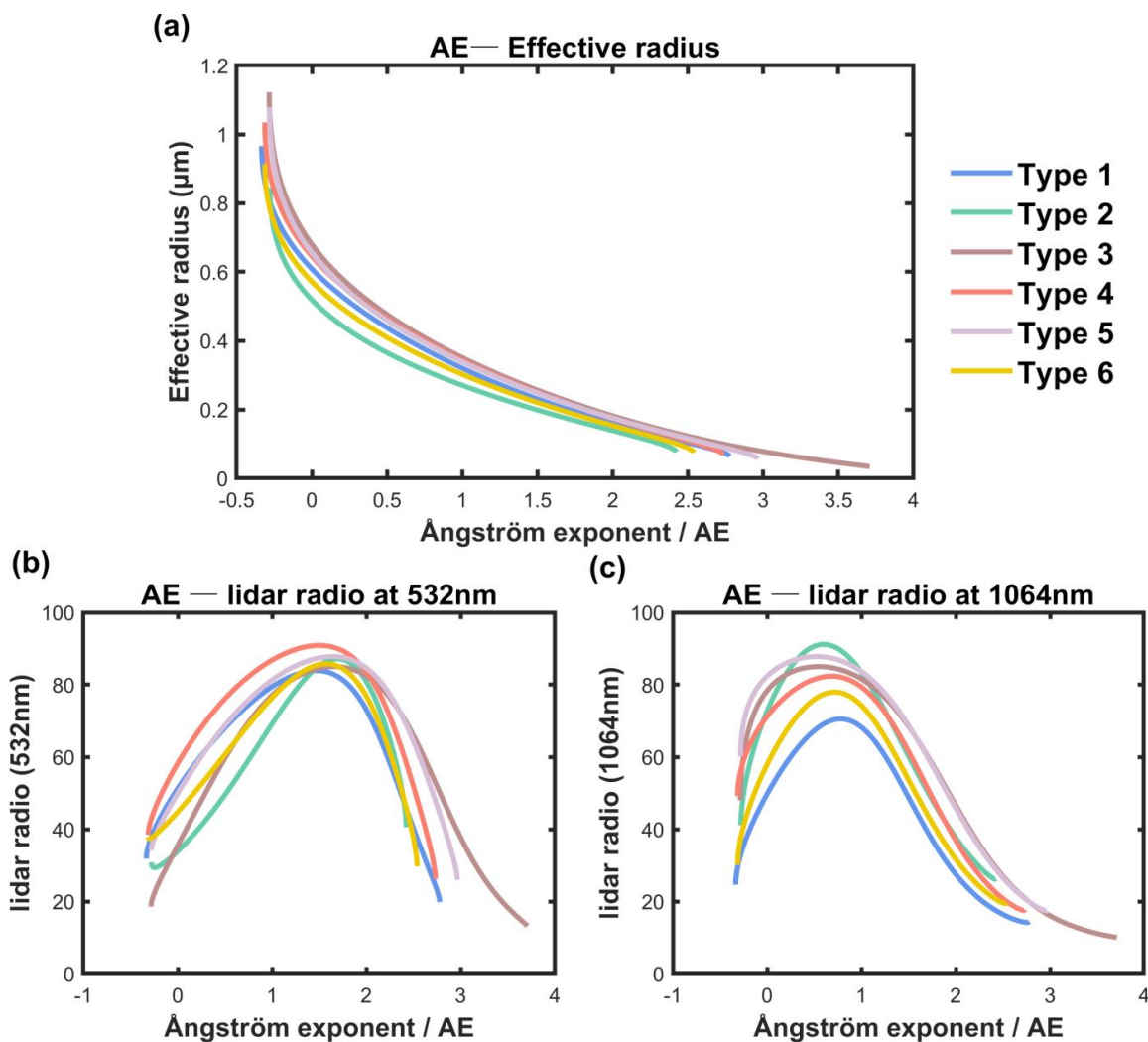
396



397 **Table 2.** Information of collocated EARLINET and CALIPSO cases.

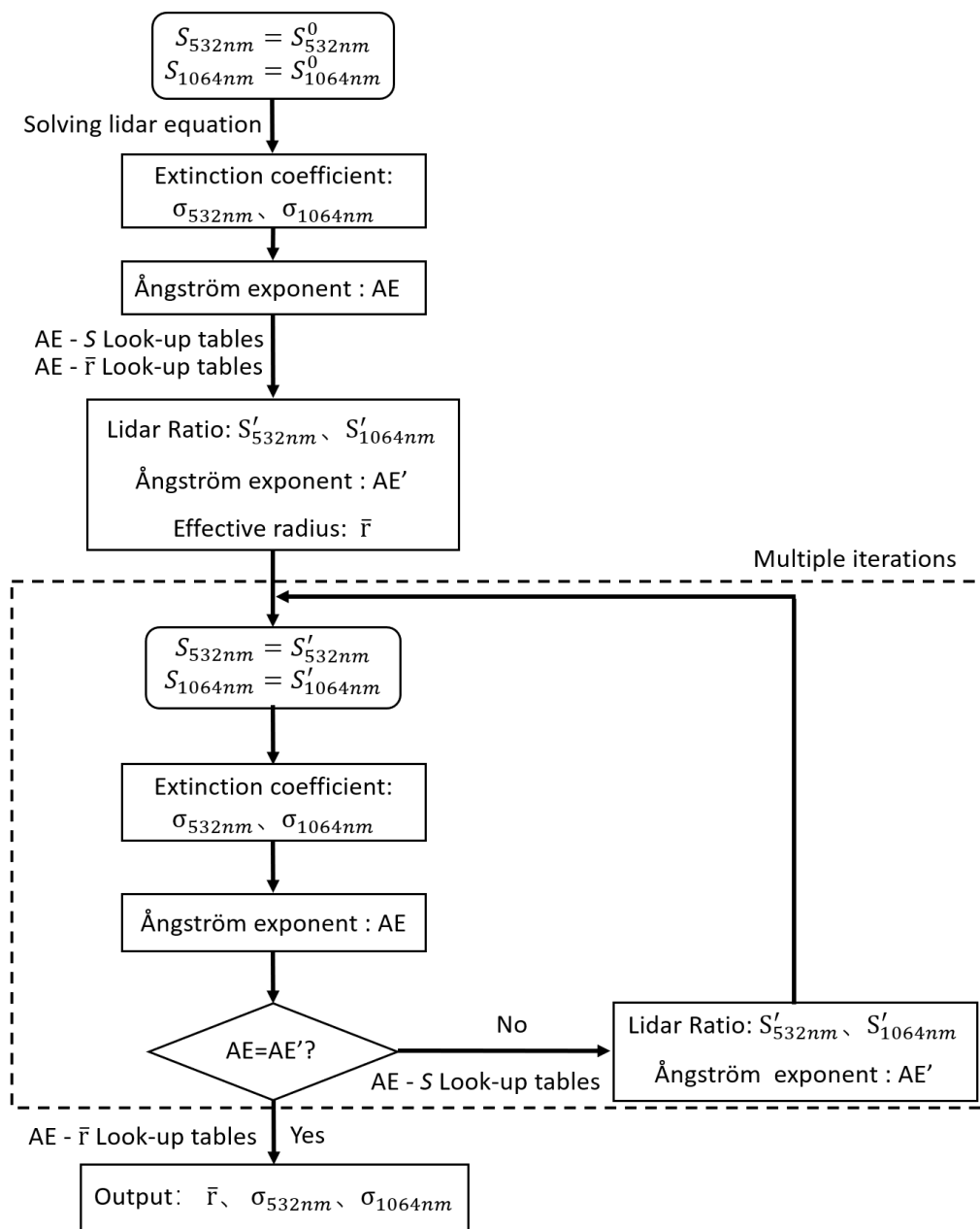
398

<b>Station</b>	<b>Time (UTC)</b>	<b>Horizontal distance (km)</b>
Napoli	2006-08-20 01:17:25	0.0708
	2007-06-20 01:17:57	0.0808
	2008-07-08 01:18:43	0.0690
	2008-08-02 01:13:02	1.3246
	2008-08-09 01:19:14	0.0807
	2009-09-29 01:21:03	0.0778
Evora	2019-04-05 02:47:48	0.0863
	2020-01-13 02:54:00	0.0164
	2020-03-18 02:55:43	0.0009
Warsaw	2015-08-15 01:19:14	< 0.0001
	2020-03-31 01:13:38	0.0177



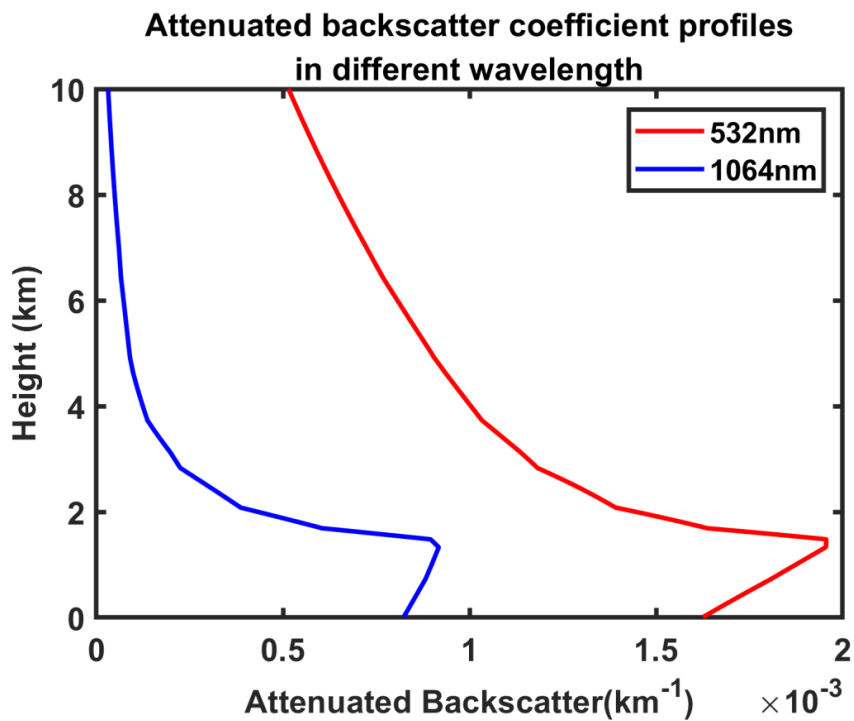
399

400 **Figure 1.** The Look-up tables for (a) AE-effective radius, (b) AE-lidar ratio at 532nm and (c) AE-lidar ratio  
401 at 1064nm. The AE is calculated using 532nm and 1064nm aerosol extinction coefficients.



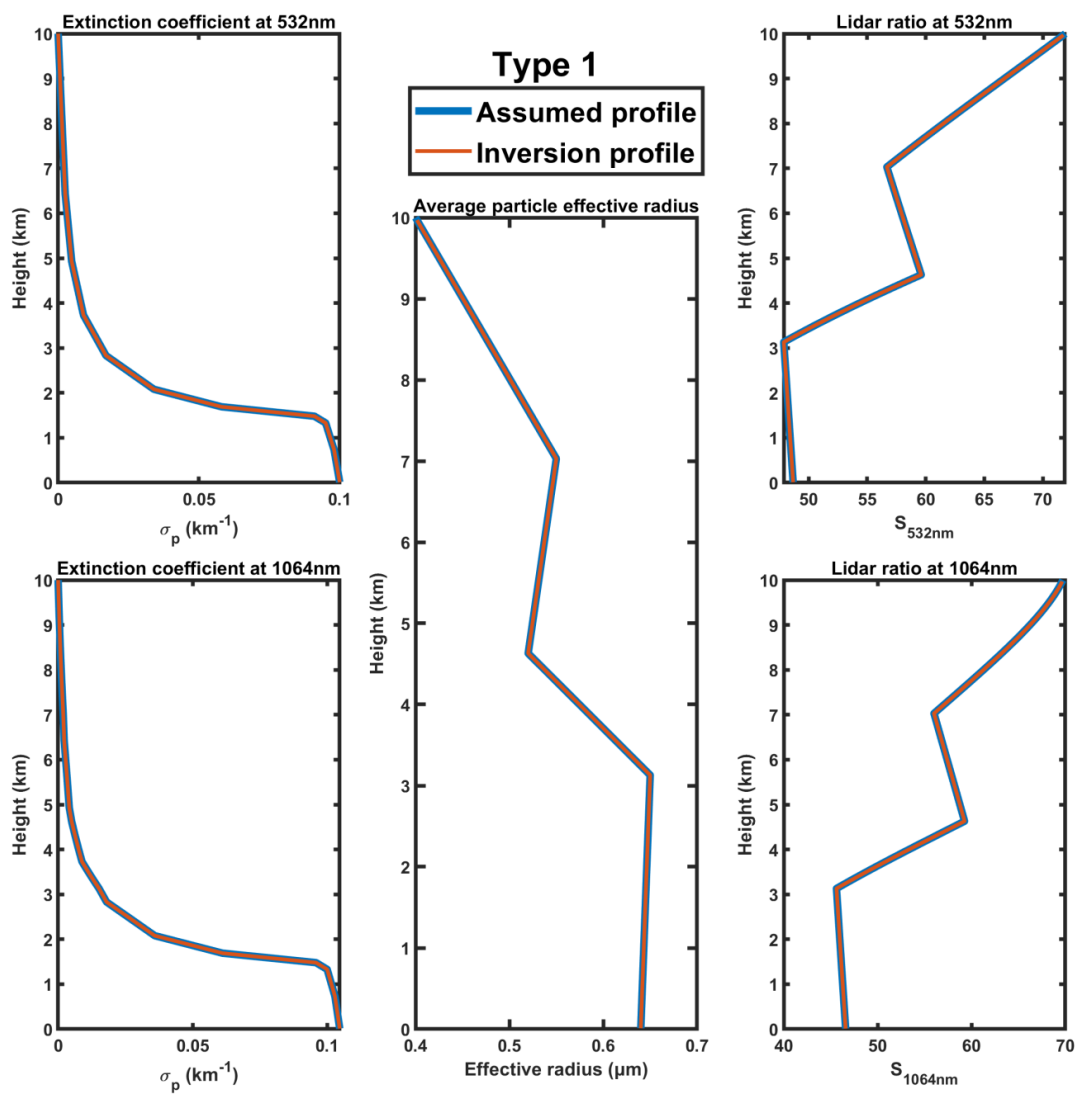
402

403 **Figure 2.** Schematic of the inversion algorithm ( $\lambda_1$  and  $\lambda_2$  represent the two different wavelengths,  
 404 respectively; S is the lidar ratio;  $\sigma$  is the aerosol extinction; AE is the Ångström index;  $\bar{r}$  is the average  
 405 particle effective radius;  $S^0$  is the initial value of lidar ratio;  $S'$  and  $AE'$  are the look up values of lidar ratio  
 406 and Ångström index, respectively.)



407

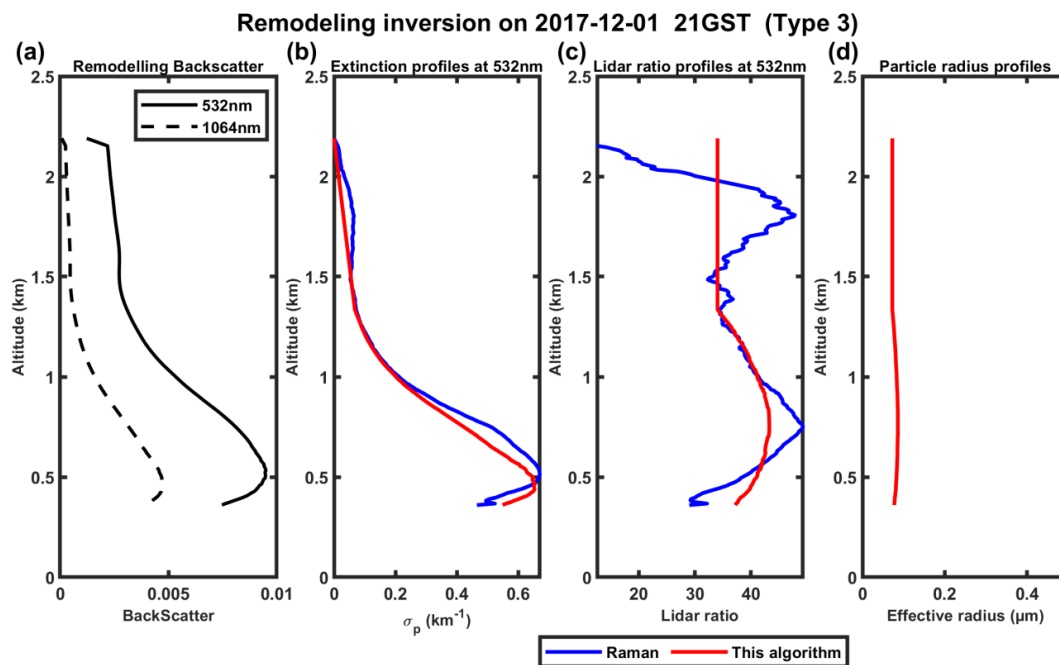
408 **Figure 3.** The attenuated backscatter coefficient profiles at different wavelengths using synthetic data.



409

410 **Figure 4.** The result of the inversion algorithm using the synthetic data shown in Figure 3.

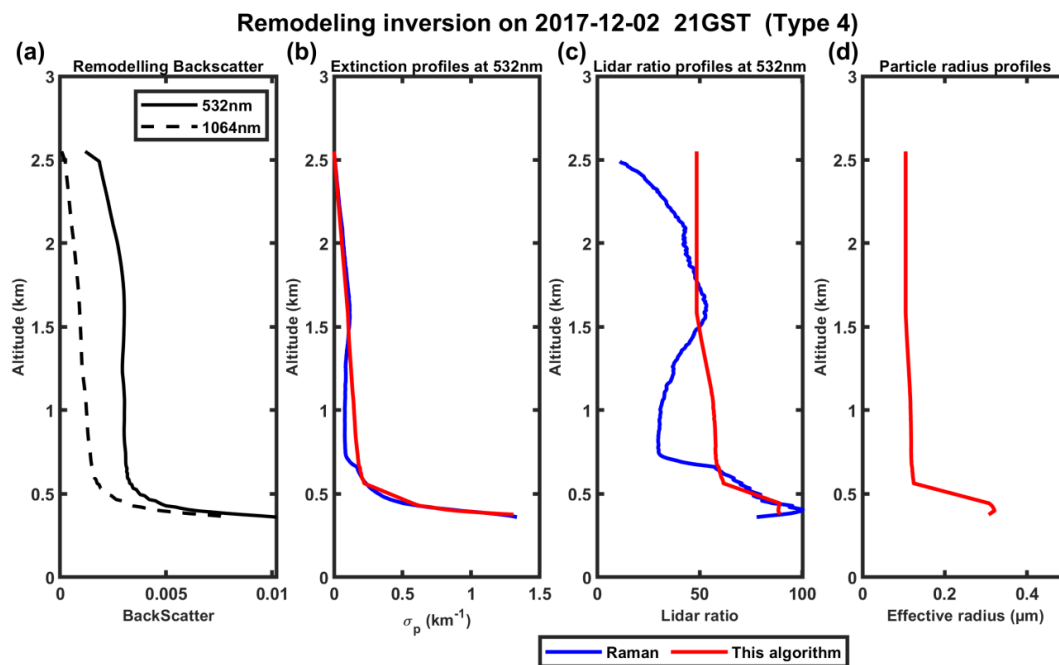




411

412 **Figure 5.** (a) Remodeled downward attenuated backscatter profiles measured by Raman lidar in PKU on 1  
413 December 2017; (b) show the extinction profiles inverted by the modified inversion algorithm (red) and  
414 Raman (blue); (c) shows the particle effective radius profiles.

415

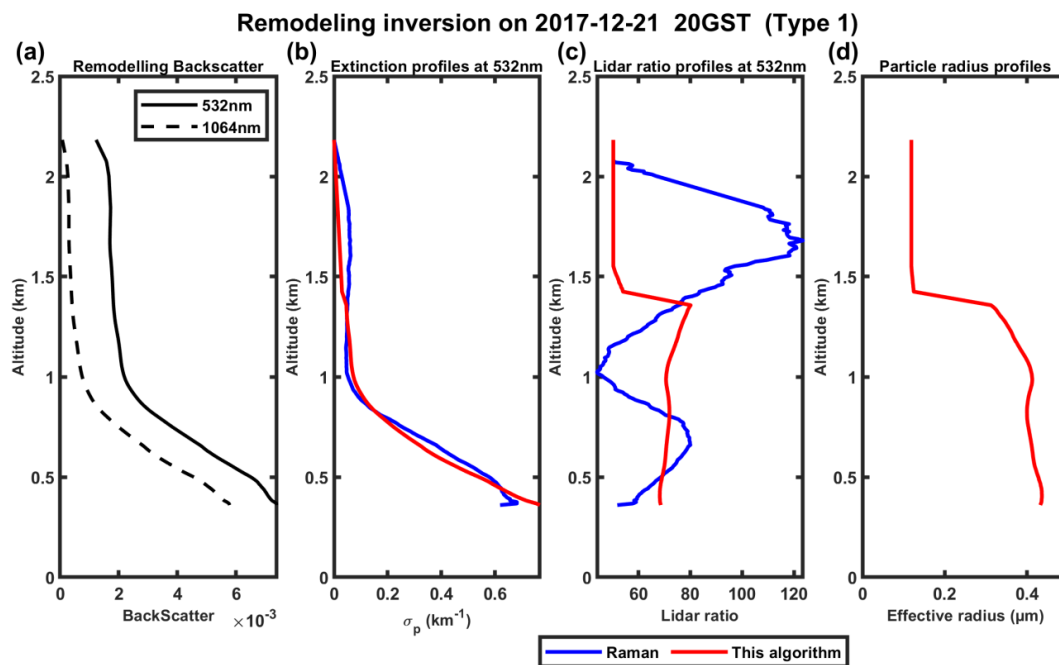


416

417

418

**Figure 6.** Same as Figure 5 but on 2 December 2017.

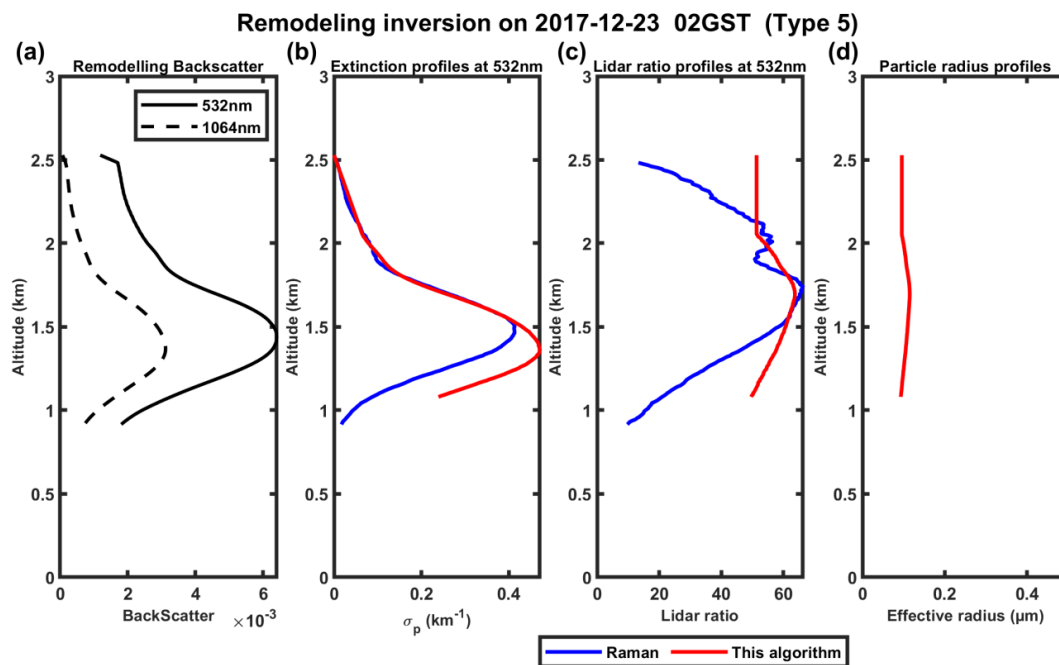


419

420

421

**Figure 7.** Same as Figure 5 but on 21 December 2017.

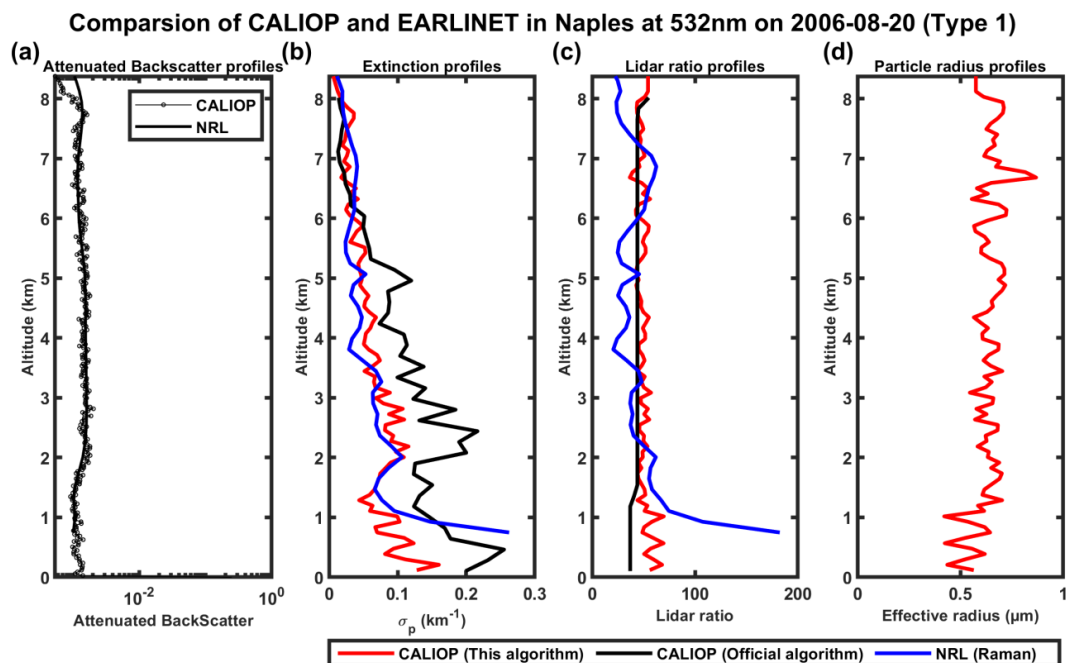


422

423

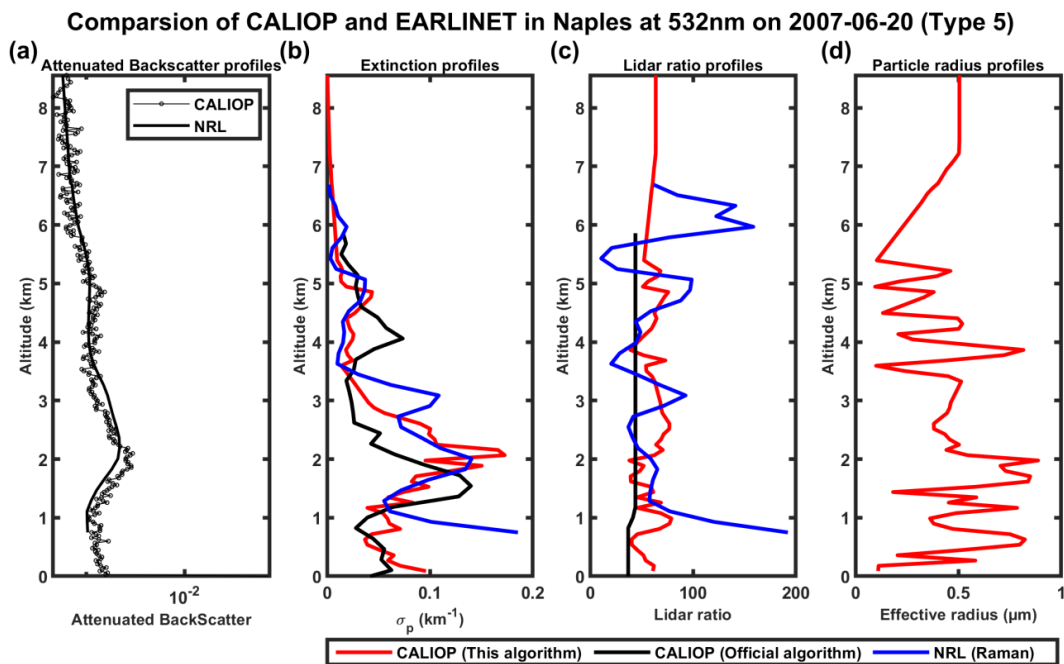
424

**Figure 8.** Same as Figure 5 but on 23 December 2017.



425

426 **Figure 9.** 532nm and 106 nm attenuated backscatter profiles measured by CALIOP (black solid line with  
427 circle marker) and NRL (remodeling, black solid line) on 20 August 2006 in logarithmic scale in horizontal  
428 direction (a); (b, c, d) show the extinction profiles, lidar ratio profiles and particle radius profiles,  
429 respectively, provided by our inversion algorithm (red), CALIOP operational level 2 product (black) and  
430 EARLINET level 2 product (blue).

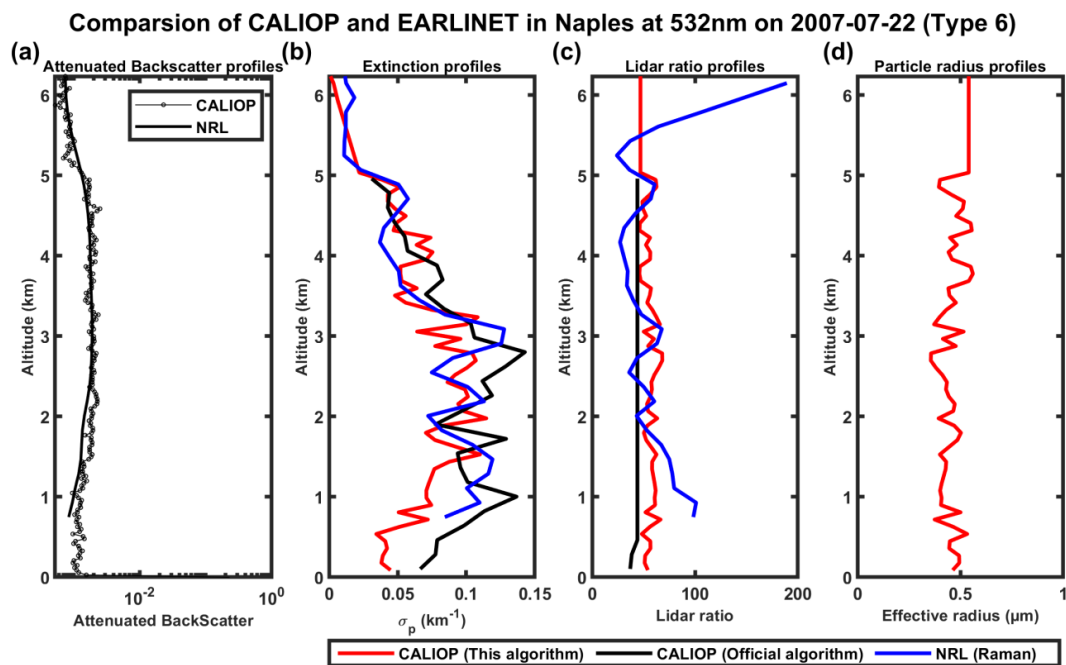


431

432

433

**Figure 10.** Same as Figure 9 but on 20 June 2007.



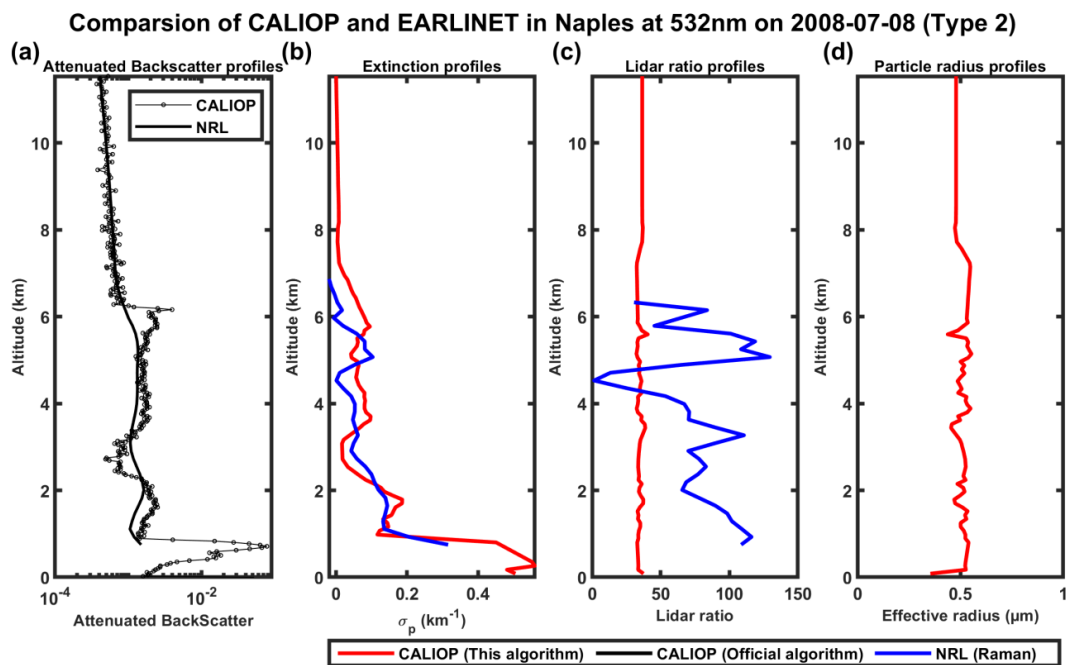
434

435

436

437

**Figure 11.** Same as Figure 9 but on 22 July 2007.



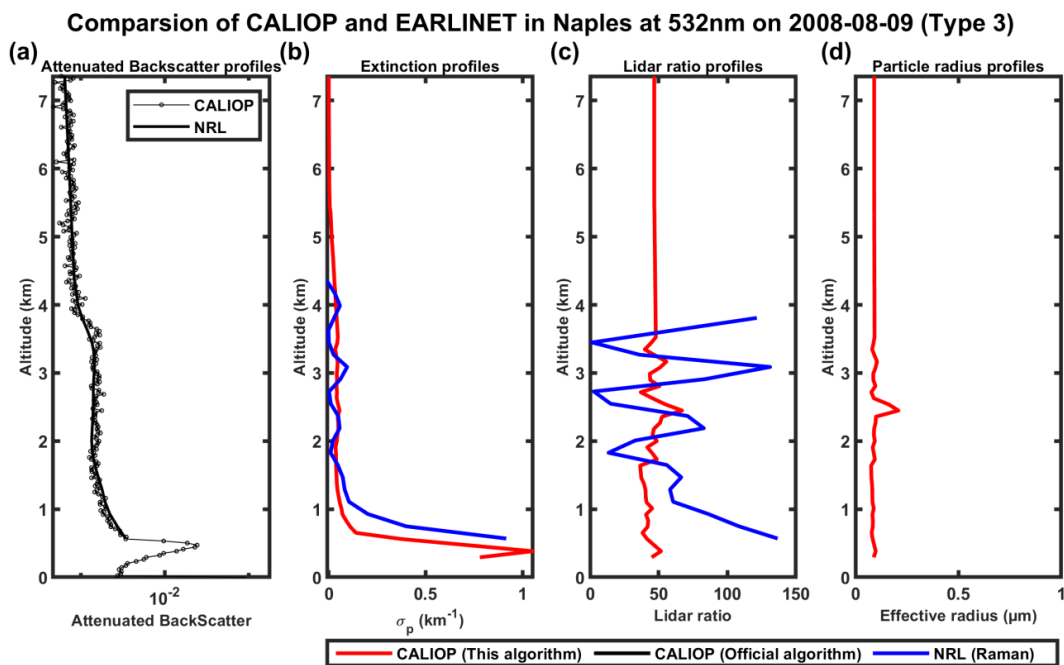
438

439

440

**Figure 12.** Same as Figure 9 but on 8 July 2008.



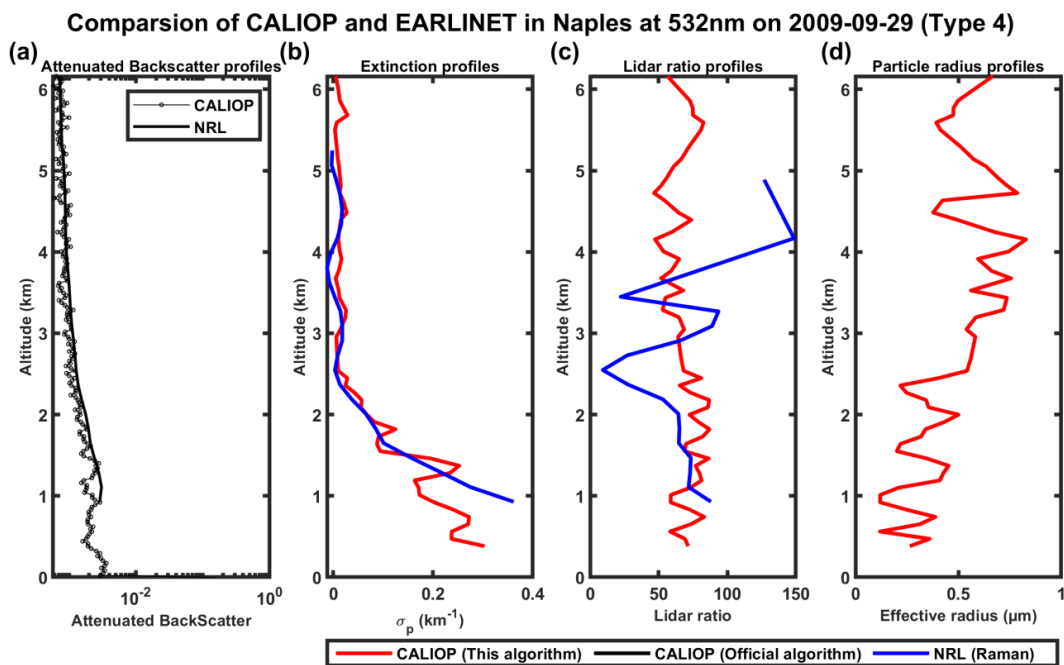


441

442

443

**Figure 13.** Same as Figure 9 but on 9 August 2008.

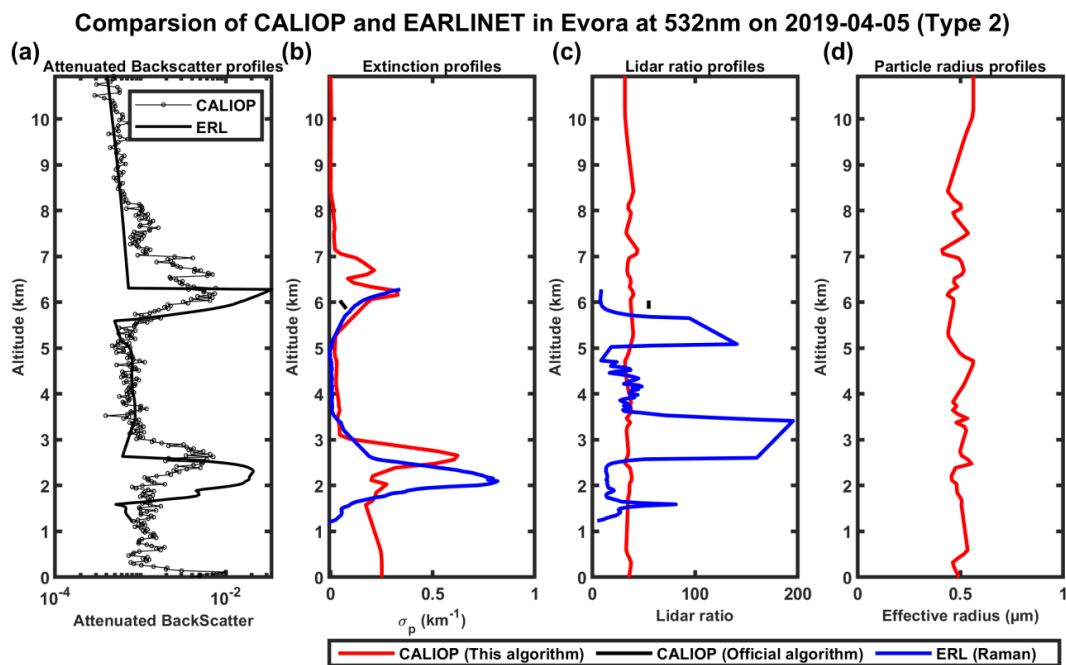


444

445

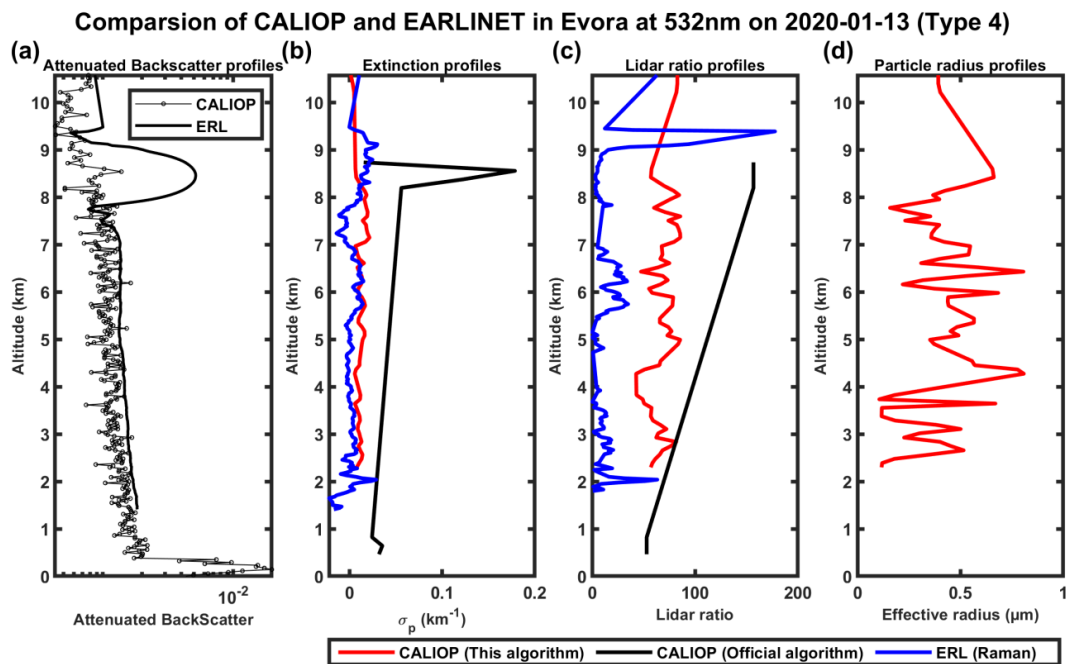
446

**Figure 14.** Same as Figure 9 but on 29 September 2009.



447

448 **Figure 15.** 532nm and 106 nm attenuated backscatter profiles measured by CALIOP (black solid line with  
449 circle marker) and ERL at the Evora station (remodeling, black solid line) on 20 August 2006 in  
450 logarithmic scale in horizontal direction (a); (b, c, d) show the extinction profiles, lidar ratio profiles and  
451 particle radius profiles, respectively, provided by the modified inversion algorithm (red), CALIOP level 2  
452 (black) and EARLINET level 2 (blue).

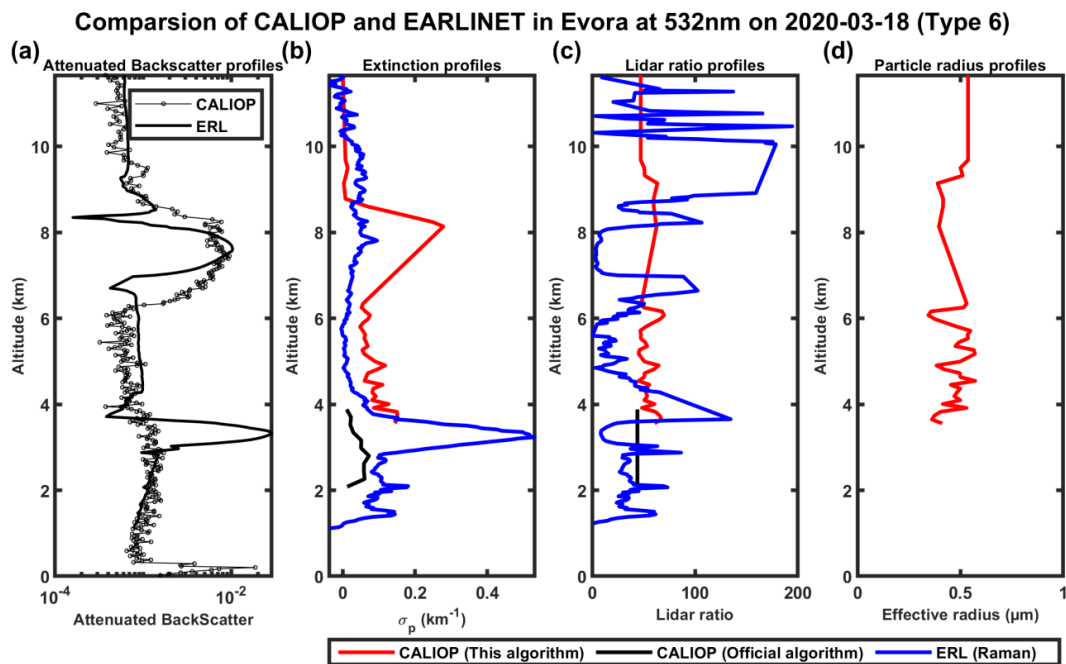


453

454

455

**Figure 16.** Same as Figure 15 but on 13 January 2020.

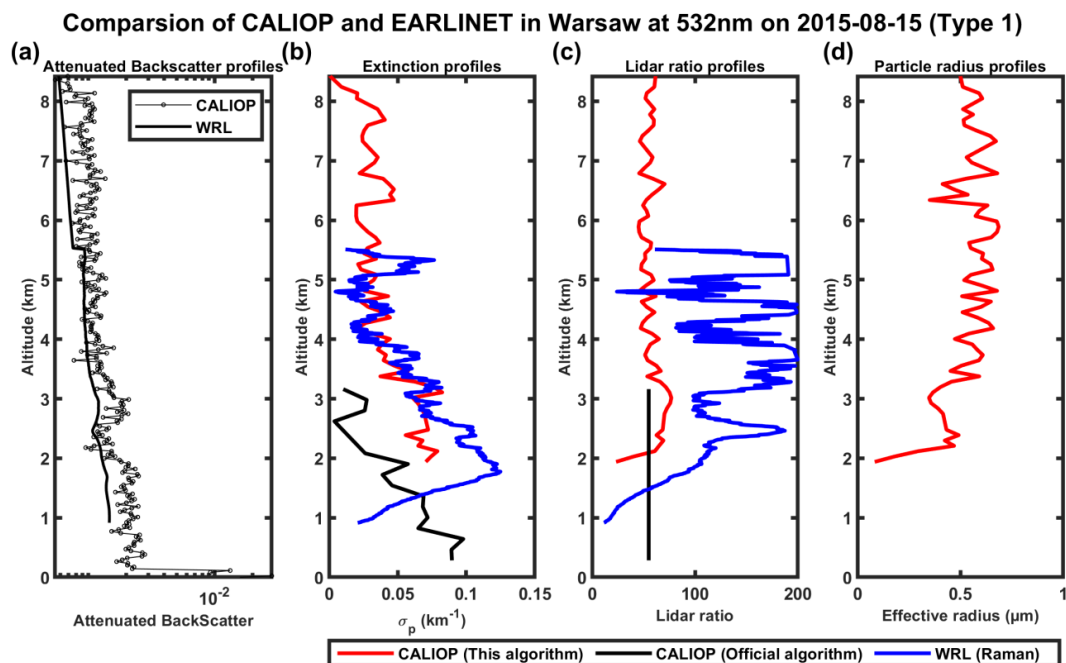


456

457

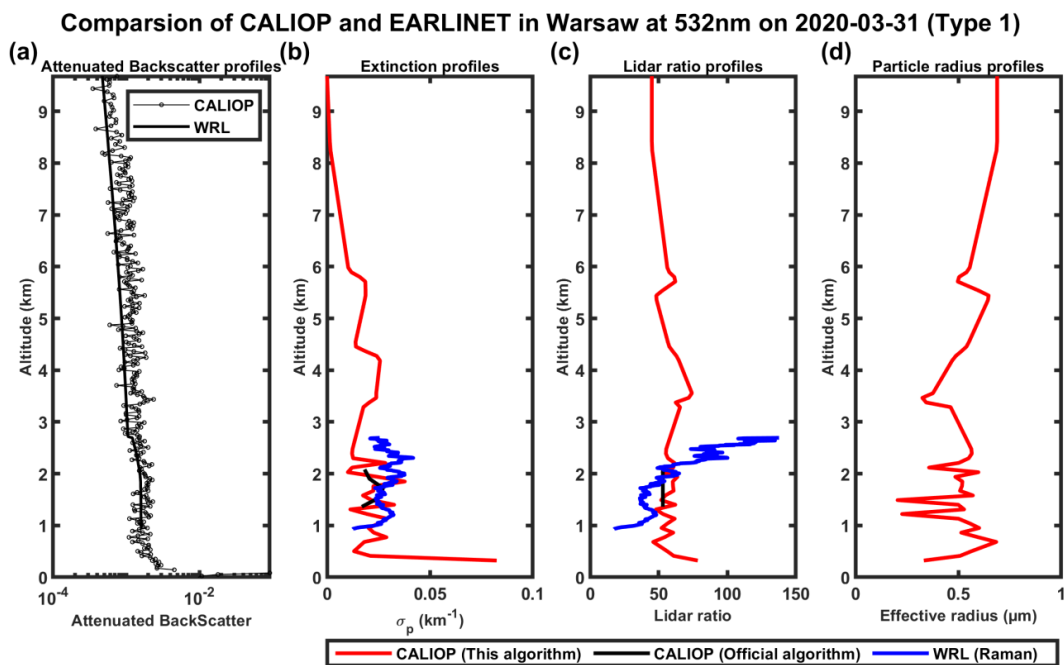
458

**Figure 17.** Same as Figure 15 but on 18 March 2020.



459

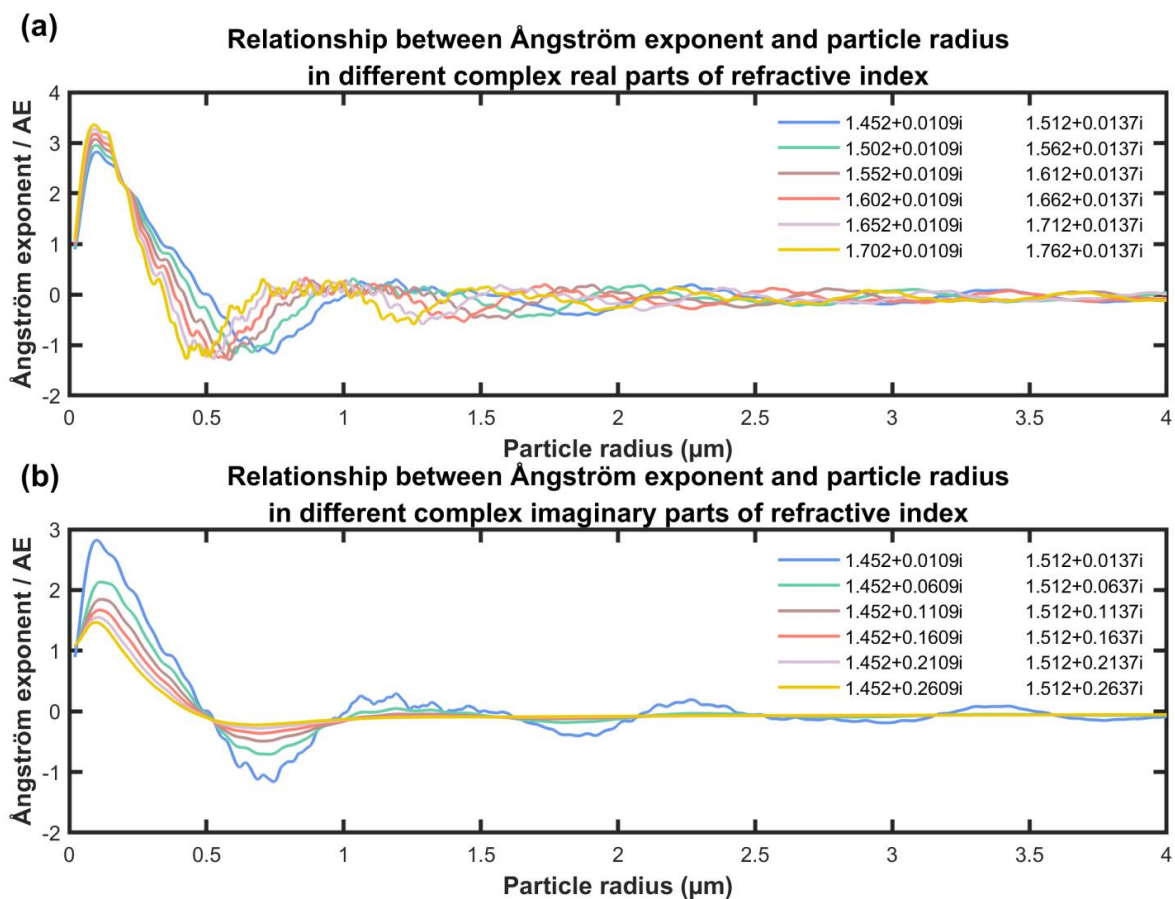
460 **Figure 18.** 532nm and 106 nm attenuated backscatter profiles measured by CALIOP (black solid line with  
461 circle marker) and WRL at the Warsaw station (remodeling, black solid line) on 20 August 2006 in  
462 logarithmic scale in horizontal direction (a); (b, c, d) show the extinction profiles, lidar ratio profiles and  
463 particle radius profiles, respectively, provided by the modified inversion algorithm (red), CALIOP level 2  
464 (black) and EARLINET level 2 (blue).



465

466

**Figure 19.** Same as Figure 18 but on 31 March 2020.



467

468

469

**Figure 20.** The effect of the complex refractive index on Ångström exponent.